Journal of Petroleum Science and Engineering 196 (2021) 107720

Contents lists available at ScienceDirect

Journal of Petroleum Science and Engineering

journal homepage: http://www.elsevier.com/locate/petrol

Modified discrete element method (MDEM) as a numerical tool for cement sheath integrity in wells

Sohrab Gheibi [a,*], Nicolaine Agofack [b], Sigbjørn Sangesland [a]

[a] Norwegian University of Science and Technology (NTNU), Trondheim, Norway
[b] SINTEF Industry, Trondheim, Norway

ARTICLE INFO

Keywords:
Cement sheath integrity
Hydration
Fracture
Debonding
Casing pressure

ABSTRACT

Cement sheaths undergo extreme loading conditions in wells during subsurface operations. A damaged cement sheath may lead to fluid communication between different formation layers and fluid migration up to the surface, which can cause environmental, technical, and economic problems. In this study, we numerically analyze cement sheath stability using the modified discrete element method (MDEM). MDEM considers the cement sheath and rock formation as porous media and can model discontinuous fracturing of the materials. Analyses are performed based on a small-scale cement sheath integrity test and field cement pressure data measured by Cooke et al. (1983). Oil well class H cement was used, and its poroelastic properties were estimated using a micromechanics model and a multi-scale homogenization technique. First, the evolution of the stress state was approximated in the cement sheath and rock formation. Then, radial fracturing, shear failure, and interface debonding formation were studied under pressure increase/decrease operations. The effects of several parameters, such as the casing size, rock elastic parameters, and loading time, were also investigated. During the hydration of cement, the compressive and shear stresses evolved in the cement sheath, and the stresses in the surrounding formation also changed. The simulation results showed that a decrease in the casing pressure can lead to debonding of the casing-cement interface, and the calculated interface opening was within 1–50 μm. A pressure increase in the casing can lead to progressive shear and tensile failures in the cement sheath. A further pressure increase did not extend those failures into the rock formation; rather, it increased the number of radial fractures in the cement sheath. The analyses showed that a lower decrease and increase in the casing pressure is required to generate debonding and radial fracture in the cement sheath, respectively, in the early stages of hydration after the cement is set. This is also the case when the casing has a larger diameter and smaller thickness. When the cement sheath is bonded to a softer rock formation, the pressure increase required to create a fracture in the cement is lower compared with the case in which the sheath is bonded to a stiffer formation. However, in the case of softer formation, debonding was not observed.

1. Introduction

In the oil and gas industry, wells are used for the exploration or production of hydrocarbons in underground formations. A hole is drilled downward from the surface with an appropriate drill bit, and mud with a suitable density is simultaneously introduced to cool down the drill bit, carry the cuttings, and keep the wellbore from collapsing. After drilling a section, a casing is run into the well filled with mud. The cement slurry is then pumped to displace the mud and to fill the space between the casing and the rock formation. The cement slurry is allowed sufficient time to harden and form the cement sheath. The principal functionalities of the cement sheath are to prevent formation fluid from penetrating the annulus space, to provide zonal isolation, to act as a mechanical support, and to protect the casing against corrosive substances. During its lifetime, the cement sheath undergoes various mechanical and thermal loadings as during a casing test, or when injecting or producing a fluid at different temperature. These loads can damage the cement sheath and compromise its integrity.

In order to study the cement integrity, small-scale experiments (e.g., Goodwin and Crook, 1992) and large-scale experiments (e.g., Therond et al., 2017) were performed to understand casing-cement-formation behavior in terms of the cement's integrity. Goodwin and Crook

* Corresponding author.
E-mail address: sohrabgheibie@gmail.com (S. Gheibi).

https://doi.org/10.1016/j.petrol.2020.107720
Received 15 April 2020; Received in revised form 27 June 2020; Accepted 29 July 2020
Available online 14 August 2020

(1992) carried out a pressure increase/decrease experiment of the cement sheath. Jackson and Murphey (1993) performed similar experiments and concluded that flow occurs when the pressure in the casing decreases to 1000 psi (6.9 MPa) after being increased up to 8000 psi (55 MPa). However, the flow stops after the pressure is increased to 2000 psi (13.8 MPa) afterwards. During the pressure reduction test, they observed that the flow started after the casing pressure was decreased from 10,000 psi (69 MPa) to 3000 psi (20.7 MPa) and 2000 psi (13.8 MPa) for an applied differential pressure in the annulus of 100 psi (0.69 MPa) and 10 psi (0.069 MPa), respectively. Boukhelifa et al. (2004) also investigated properties of different cements by simulating the expansion and contraction of the casing and measuring the flow in the annulus as a result of tensile and debonding failures. Li et al. (2016) investigated the failure mechanism of the cement sheath under down-hole pressure and temperature conditions using an experimental wellbore simulator. A computed tomography (CT) scan of the sampled cement sheath showed an obvious difference in the particle distribution in the radial direction after the test. The sample tested under high confinement showed a pore volume reduction. Therond et al. (2017) used a large-scale apparatus to study the cement integrity under controlled conditions of pressure and temperature. They observed that the greatest increase in the permeability of the annulus was due to the formation of a microannulus, while the tensile radial fractures did not have a significant impact on the permeability increase. They also reported that the microannulus formed because of cooling of the well was closed after the well was heated up again. Skorpa et al. (2018) carried out pressure test experiments of a casing-cement-rock system by combining X-ray and CT, and they observed the penetration of the tensile fracture into the formation. In another study, they also investigated the effect of mud film on cement integrity (Skorpa et al., 2019). Bu et al. (2020) designed a setup for testing the radial bond strength of a cement-casing interface. The test results showed that the interface radial bond strength was greater for a higher curing temperature and lower formation water content.

Several numerical and analytical approaches are used to assess the cement sheath integrity. Thiercelin et al. (1998b) developed an analytical solution to calculate stresses caused by pressure test and temperature changes in the cement for failure analyses. Bosma et al. (1999), Ravi et al. (2002), and Gray et al. (2009) applied finite-element modeling in the stability of well and cement integrity, and they investigated the effect of different loading scenarios and cement type on the cement sheath failure.

Thiercelin et al. (1998a) adopted the finite-element method and modified Cam-clay, and they related the bulk shrinkage of cement paste to the pore pressure reduction due to hydration. They estimated the evolution of the stresses in the cement sheath. Fourmaintraux (2005) used the system response curve (SRC), decomposing the well into different components, and they found the stresses in the casing-cement-formation under mechanical equilibrium conditions. They emphasized the effect of pore pressure of the cement paste on the shrinkage and failure analyses of the cement. Gholami et al. (2016) used a thermo-poroelastic and numerical approach to assess the integrity of the cement sheath, and they concluded that a thicker cement sheath maintains its integrity against a higher load applied by the formations.

Wang and Dahi Taleghani (2017) developed a coupled three-dimensional (3D) poroelastic finite-element model with embedded cohesive zones to simulate fracture propagation along the wellbore during hydraulic fracturing operation. Arjomand et al. (2018) used a 3D finite-element model to investigate the effect of orientation of in-situ stresses, formation stiffness, and eccentricity of the casing on the well integrity. Bois et al. (2019) presented a thermo-chemo-poro-elasto-plasticity model, which considers the cement paste as a porous media that evolves with time. The shrinkage of the cement was related to the thermal and pore pressure changes. Their model was able to predict the pore pressure as well as the initial stresses in the cement. It was used to evaluate the cement-plug integrity (Bois et al., 2019) and in the modeling of gas migration to prevent sustained casing pressure (Vu et al., 2018). Wise et al. (2020) performed finite-element analysis and concluded that the wellbore size and casing thickness were the most important parameter in the formation of microannuli.

It is important to have a knowledge of the correct stress state in the cement. As discussed by Bois et al. (2011), the stress state not only determines when the cement sheath can fail, but also the type of compressive or tensile failure mechanisms. Therond et al. (2017) used a simulator based on a thermo-chemo-poro-elasto-plastic approach to estimate the stress state evolution, shrinkage, and cement pore pressure versus the degree of hydration. Recently, Agofack et al. (2020) presented a chemo-poro-elastoplastic model capable of predicting the stress-strain behavior of an oilwell cement, its macroscopic shrinkage, its initial stress estimation as well as a possible creation of microannulus during cement hydration under various conditions of temperature and pressure.

In this paper, we present a discrete element-based approach to analyze the integrity of the cement sheath. One advantage of this approach over some other approaches in the literature is that the developed methodology considers the cement sheath and the formation as porous media. The other advantage is that the cement is an aging material and poroelastic properties are estimated using the micromechanical methods. Moreover, the discrete nature of the model enables the introduction of pre-existing cracks and the evolution of discrete fractures in the model. The model is within the framework of poromechanics which relate the pore pressure, the effective stress, as well as the poroelastic properties and compaction of an aging cement.

A brief overview of the used simulator is highlighted in Section 2. The procedure of the modeling is explained in Section 3, while Section 4 focuses on the presentation of the results of the small- and large-scale analyses. Some conclusions are presented in Section 5.

2. Numerical model

This section discusses the stress and failure analysis of the cement sheath. Modified Discrete Element Method (MDEM) was adopted to perform stress and failure analyses in this paper. MDEM is a hybrid code that captures both materials continuum and discontinuum features. In the elastic regime, the continuum part is active which is equivalent to the finite element method and as soon as the failure criterion is met the discontiuum feature is activated and fractures form. A triangle continuum element is composed of three springs and breakage of these springs lead to formation of fractures. More details are given in the appendix.

In the literature, there are three types of approaches that relate to the stress in the cement sheath. The first approach proposes zero stress in the cement, and has been used by some authors (Thiercelin et al. 1998b; Bosma et al., 1999). In the second approach, the stress in the cement is assumed to be constant and equal to the hydrostatic pressure of the cement slurry column (Bosma et al., 1999; Gray et al., 2009). The third approach considers that the stress in cement changes with hydration as the cement paste moves from the liquid to solid phase (Thiercelin et al., 1998a; Bois et al., 2019). In this study, only the first and third approaches are considered.

2.1. Zero stress in the cement

The assumption of zero stress is hardly defendable, especially in downhole conditions. It is carried out here only to validate the model against the analytical solution of Thiercelin et al. (1998b). The geometrical parameters of the well were taken from Thiercelin et al. (1998b), and consisted of a drill bit with diameter 215.9 mm (8.5″), and outer and inner casing diameters of 177.8 mm (7″) and 152.4 mm (6”), respectively. Similarly, the Young moduli and Poisson ratio of the casing, cement, and the rock formation were 200 GPa and 0.27, 5 GPa and 0.2, and 10 GPa and 0.2, respectively. In the model, the initial in-situ stress was zero. Later, the inner wall of the casing was pressurized up to 1000 psi (6.9 MPa). Fig. 1 shows the radial and tangential stresses

along the radial direction, and there was an excellent match between our results and those of Thiercelin et al. (1998b).

2.2. Progressive evolution of stress in the cement

The results are based on the fact that during cement hydration, the pore pressure of the cement paste progressively decreases, leading to shrinkage and compaction of the cement particles (Agofack et al., 2019, 2020). At each step of hydration, the poroelastic parameters of the cement change. As reported by Cooke et al. (1983), Samudio (2017), and Agofack et al. (2020), the pressure reduction profile in a given cement paste depends on the in-situ conditions of hydration, such as pressure, temperature, or water supply from the environment.

In this paper, the pressure profile that is used was obtained from Cooke et al. (1983) for a class H oil-well cement. Because cement poroelastic properties change during hydration and are necessary in the modeling, a micromechanics model coupled with homogenization techniques are used to estimate these parameters during hydration. The procedure and main equations, which were detailed in Agofack et al. (2019), are briefly described in the next section. Because the simulation from homogenization techniques presents the poroelastic parameters as a function of the degree of hydration, and the in-situ measured pressure profile is given as a function of time, the degree of hydration as a function of time is needed. This was done using an approach based on Pang (2011).

The methodology used in this paper is explained step-by-step as follows:

i. Initial in-situ stress and pore pressure installation: A rectangular model is constructed in the code, and the stress boundary conditions (isotropic or anisotropic) are applied to the model boundaries. The pore pressure value is then initiated, and the model is run to reach the mechanical equilibrium.
ii. Well drilling: The well domain is drilled, and the model is run to reach the equilibrium. The drilling leads to a new stress state in the model. In principle, failure can appear in the rock formation in the well vicinity.
iii. Mud weight installation: The resultant pressure of the mud is applied on the wall of the well to provide temporary mechanical support, and the model is run to reach the equilibrium.
iv. Casing installation: The casing domain is activated in the model. Similarly, the casing is under mud weight pressure. The model is run to reach the equilibrium state of the entire system.
v. Cementing: The mud pressure is replaced by the cement slurry pressure, and the model is run to reach the equilibrium.
vi. Cement hardening: The cement domain is activated with the bulk modulus Kξ, shear modulus Gξ, and pore pressure Pcξ at the degree of hydration ξ. The model is then run to reach equilibrium. This step is repeated from an initial value ξ0 to a certain hydration degree of interest ξi, with an increment of dξ. The cement domain deforms at ξ when the pressure at this degree of hydration changes. Therefore, the change in stress depends on the deformation amplitude and the poroelastic properties of cement at ξ. This change in stress modifies the previous equilibrium condition, and the model is run to reach the equilibrium state with new states of stress and strain. If the stress state fulfils the failure criterion of the cement or that of the rock formation, failure occurs.
vii. Well pressure reduction: Owing to variations in the mud pressure, such as the use of a lighter well completion fluid, the pressure in the casing is decreased incrementally to a desired level, and the model is run to reach the equilibrium.
viii. Well pressure increase: The required pressure level is applied to the casing's inner wall, and the model run to reach the equilibrium. The pressure is applied incrementally to keep the model stable.

3. Estimation of poroelastic properties of class H during hydration

Cement paste is an evolving material. Initially behaving as fluid with suspension – zero shear modulus, and a bulk modulus at around 4 GPa (Agofack et al., 2019) – the cement paste changes progressively through complex chemical reactions, to become a solid porous material with a nonzero shear modulus. Its poroelastic properties are different at every stage of hydration. Therefore, throughout the hydration, it is almost impossible to measure these properties using conventional lab mechanical experiments such as triaxial compression or uniaxial strength tests. Thus, multi-scale micromechanical models coupled with homogenization techniques are commonly used to access the properties of such evolving materials (Bernard et al., 2003; Dormieux et al., 2006). The main equations, which are presented in previous publications (Ghabezloo, 2010; Agofack et al., 2019; Agofack et al., 2020), are briefly presented herein.

Given the material of Fig. 2 composed of n homogeneous phases, which consist of one pore phase and $m = n - 1$ solid phases, a given phase r, which is considered isotropic and with a volume fraction f_r, has k_r and g_r as bulk and shear moduli, respectively. The bulk drained modulus and the shear modulus of the material are estimated from those of its phases. The homogenized expressions of these bulk drained and shear moduli are given by the following relation:

$$K_d^{\hom} = \sum_{r=1}^{n} f_r k_r A_r^v \quad ; \quad G^{\hom} = \sum_{r=1}^{n} f_r g_r A_r^d \tag{1}$$

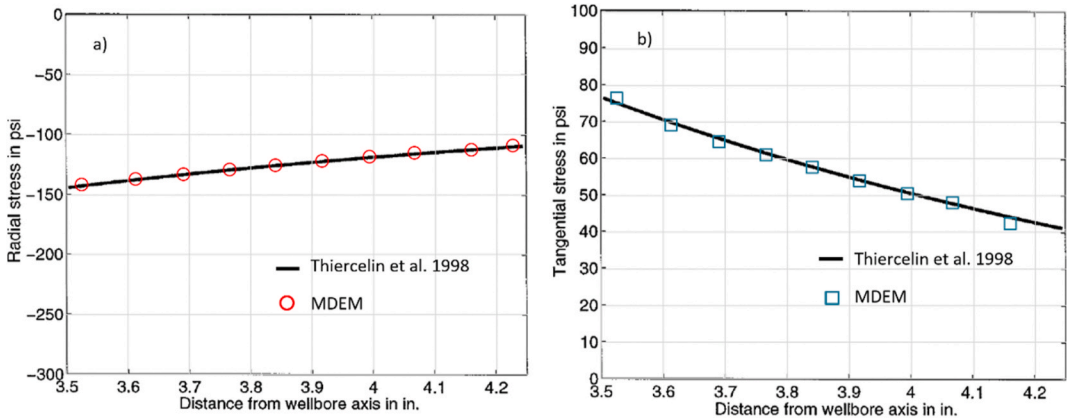

Fig. 1. Comparison between our results obtained using MDEM and those of Thiercelin et al. (1998b) for zero stress in cement: a) Radial stress and b) tangential stress profile in the cement as a function of distance from the centre of the well.

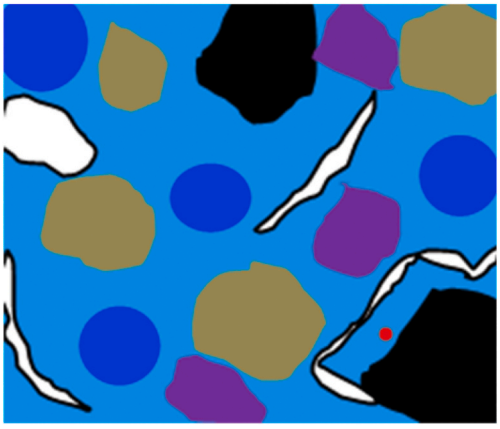

Fig. 2. Microstructure of a heterogeneous porous material composed of n homogeneous phases.

where A_r^v and A_r^d are respectively the volumetric and deviatoric coefficients of tensor known as a tensor of localization of strain, of phase r of the material microstructure. These coefficients are functions of the tensor of the reference medium c0(k0, g0). For spherical inclusions in the reference medium and under the assumption that all phases are isotropic, the following expressions are given:

$$A_r^v = \frac{[1+\alpha_0(k_r/k_0-1)]^{-1}}{\sum_r f_r[1+\alpha_0(k_r/k_0-1)]^{-1}} \tag{2}$$

$$A_r^d = \frac{[1+\beta_0(g_r/g_0-1)]^{-1}}{\sum_r f_r[1+\beta_0(g_r/g_0-1)]^{-1}} \tag{3}$$

$$\alpha_0 = \frac{3k_0}{3k_0+4g_0}; \beta_0 = \frac{6(k_0+2g_0)}{5(3k_0+4g_0)} \tag{4}$$

where k0 and g0 are its bulk and shear moduli of the reference medium, respectively. The tensors of Biot's effective coefficients and of the Biot's modulus are given by

$$b^{\text{hom}} = 1 : \left(I - \sum_{r=1}^{m} f_r \langle A \rangle_{V_r}\right); \frac{1}{N^{\text{hom}}} = 1 : \sum_{r=1}^{m} [f_r c_r^{-1} : (1 - 1 : \langle A \rangle_{V_r})] \tag{5}$$

where **1** and **I** are identity tensors of the 2nd and 4th orders, respectively. **A** is the tensor of localization and $\langle A \rangle_{V_r}$ is its average over the volume V_r of phase r. c_r is the stiffness tensor of phase r. For a porous material exhibiting multiscale porosity, such as cement paste with micro-porosity at CSH level and macropore at cement paste level, the homogenization process is performed at different levels. At level I (lowest level), the material is composed of $l (l \leq m)$ porous phases with porosity φ_r^I and $m - l$ solid phases. φ^{II} is the porosity at level II (higher level). The total porosity, the homogenized expressions of the tensor of Biot coefficients bhom, and the homogenized expression of the Biot modulus Nhom are given by Eqs. (6)–(8):

$$\varphi = \sum_{r=1}^{l} f_r \varphi_r^I + \varphi^{II} \tag{6}$$

$$b^{\text{hom}} = 1 - \sum_{r=1}^{m} [f_r \langle A \rangle_{V_r} : (1 - b_r^I)] \tag{7}$$

$$\frac{1}{N^{\text{hom}}} = \sum_{r=1}^{m} \left[f_r \left(c_{sr}^I\right)^{-1} : (1 - 1 : \langle A \rangle_{V_r}) : \left(1 - b_r^I\right) + \frac{1}{N_r^I} \right] \tag{8}$$

where the superscripts I and II refer to parameters at level I and level II, respectively; csr is the stiffness tensor of solid matrix of phase r. When all phases at level I are non-porous, $\varphi_r^I = 0$, $b_r^I = 0$, $N_r^I = 0$, and $c_{sr}^I = c_r$.

The homogenization of class H cement is considered in this study, with a water-to-cement ratio equal to its standard value of 0.38 (Bensted, 1998). The procedure used is similar to that described in Agofack et al. (2019) for a class G. The main differences between these cement classes lie in the size of their clinker grains and the proportion of their main elements: alite (C3S), belite (C2S), aluminate (C3A) and ferrite (C4AF), where following cement chemistry C = CaO, S = SiO2, A = Al2O3 and F = Fe2O3. It is then assumed that the microstructure of class H cement consists of two levels of homogenization. At level I, the calcite silicate hydrate (C–S–H) both high density (HD) and low density (LD) considered as porous materials, is homogenized and their bulk and shear modulus are obtained. At level II, corresponding to that of cement paste, all the elements of its microstructure are assumed to have a spherical geometry. The bulk and shear modulus of C–S–H HD and LD, estimated in level I, are used to estimated homogenized parameters of cement paste.

Depending on how k0 and g0 of the reference medium are evaluated, different homogenization schemes are considered. The self-consistent scheme, which is suitable for materials such as cement paste, was considered, including the Mori-Tanaka scheme, diluted scheme, and self-consistent scheme. In our simulation, the Mori-Tanaka scheme was used at level I for C–S–H, which assumed the properties of the reference medium are similar to those of solid matrix of the material (c0 (k0, g0) = cs (ks, gs)). At level II, the self-consistent scheme was used. This scheme assumes that the properties of the reference medium are equal to that of the homogenized medium $c_0(k_0,g_0) \equiv c^{\text{hom}}(K^{\text{hom}},G^{\text{hom}})$, leading to a non-linear relation for the homogenized moduli $(c^{\text{hom}} \equiv f(c^{\text{hom}})$, which is solved by performing iterative calculations.

As the microstructure of cement change during hydration, the knowledge of the volume fraction of its different phases during hydration is needed. The following relation gives the volume fraction of the cement paste as function of that of the reactants and products of hydration (hydrates).

$$V_{CP} = \underbrace{V_w + \sum_r V_r^{CK}}_{\text{Reac tants}} + \underbrace{V_{CSH} + V_{CH} + V_{E-Afm} + V_{Cap}}_{\text{Products of hydration}} \tag{9}$$

where V_{CP} is the total volume of cement paste assumed constant during hydration, V_{Cap} is the pore volume that is not filled with water and is related to the chemical shrinkage, $V_{E-Afm}\pm$ is the volume of monosulfoaluminate, and V_{CH} is the volume of portlandite. $V_r^{CK} = (1-\xi_r)m_r^0/\rho_r$ is the volume of the clinker phase r (= C3S, C2S, C3A, and C4AF), where ξ_r is their degree of hydration, m_r is their mass fraction, and ρ_r is their density. The superscript 0 represents the initial value. The volume of hydration X (X = CSH or CH) at a given degree of hydration is $V_X = \sum_r V_X^r \xi_r$, where V_X^r is the volume of X from the hydration of the clinker element r (r = C3S, C2S, C3A, and C4AF). The total degree of hydration is given by

$$\xi = \sum_{r=1}^{4} m_r \xi_r \tag{10}$$

The volume fraction is given by $f_r = V_r/V_{CP}^0$, with r being a microstructure element and V_{CP}^0 being the initial volume of cement paste. The monosulfoaluminate is rather limited in the tested cement paste, and in our simulations, their properties of monosulfoaluminate and those of CSH are assumed to be similar. Their volume fraction is then included in that of the CSH. The bulk and shear moduli of different phases of cement paste are presented in Table 2 in Agofack et al. (2020). These moduli were used to estimate the homogenized Young modulus E, bulk drained modulus Kd, shear modulus G, the Biot coefficient b, the undrained Poisson ratio vu and the porosity of the cement paste, and they are presented in Fig. 3.

3.1. Cement properties

The cement used in Cooke et al. (1983) was class H cement with sand with a slurry density of 1983 kg/m3. However, in our simulations, the poroelastic properties of the cement used were only for the class H cement, without any addition of sand. Cooke et al. (1983) did not report more details on the cement, such as the elastic properties or the water-to-cement ratio (w/c), with the exception of the approximate setting time based on their unpublished lab tests, and which can be estimated using the curves of temperature (related to the heat of hydration), as given in Fig. 8. The homogenization presented in the previous section therefore assumed a standard w/c for class H cement. The homogenized parameters, as presented in Fig. 3 are function of the degree of hydration. However, the cement pressure measured by Cooke et al. (1983) is given as a function of time. Thus, a model of degree of hydration as function of time is needed.

The degree of hydration of cement depends on different factors, such as the cement type (cement fineness), water-to-cement ratio, as well as temperature and pressure conditions. Pang et al. (2013) proposed a methodology to obtain the unknown degree of the hydration as function of time at a given temperature and pressure, using a certain reference degree of the hydration-time relationship. A factor C is used to scale the reference case (subscripted by r in Eq. (11)) to a desired condition as:

$$C(T_r - T,\ \ P_r - P) = \exp\left(-\frac{E_a}{RT}(1 - T/T_r) + \frac{\Delta V}{RT}(P_r - P) \right) \tag{11}$$

where E_a is the apparent activation energy (J/mol), ΔV is the apparent activation volume (m3/mol), R is the gas constant (8.314 J/mol/K), T and P are respectively the temperature in Kelvin (K) and pressure in Pascal (Pa) of an arbitrary curing condition, while T_r and P_r are respectively the temperature (in K) and pressure (in Pa) of the reference curing condition, and C is the scale factor associated with the temperature change from T_r to T and the pressure change from P_r to P. A detailed derivation of the model can be found in (Pang, 2011). To obtain the degree of the hydration as function of time at a desired condition, the factor hydration time is divided by a factor C. Fig. 4 shows the degree of hydration versus time for a reference condition (13.1 MPa, 60 °C from Pang et al., 2013) and 48.95 MPa, 60 °C (scaled). As expected, pressured have little effect of the degree of hydration. However, as presented in Agofack et al. (2019), the temperature change significantly impacts the degree of hydration versus time relationship.

4. Results

4.1. Simulation of a lab-scale experiment

A small-scale casing-cement-rock system was tested by Vrålstad et al. (2019). The simulation of a two-dimensional (2D) model of the experiment is presented in this section. This simulation was performed to validate the capability of the code when modeling a small-scale experiment and to obtain the model parameters for the analysis on a large scale. The setup used by Vrålstad et al. (2019) consisted of a 2-mm-thick carbon-steel (pipe X-52) with an outer diameter of 60.3 mm (inner diameter of 56.3 mm), and a rock hollow cylinder with an internal diameter of 76 mm and a thickness of 38 mm. The cement paste was pumped into the annulus space (8 mm thick). After the hardening of the cement paste, the casing was pressurized in a stepwise manner while the setup was scanned using an X-ray CT machine. The scanning enabled the characterization of the cement and rock before and during the casing pressurization. During post-processing, a 3D image of the sample was constructed. This image also included the existing and newly formed cracks as well as initial defects on the sample. The casing pressure was increased to a certain level and then reduced, and in the next step, the casing pressure was increased to a level that was higher than the precedent and then reduced again. This was repeated until the final stage.

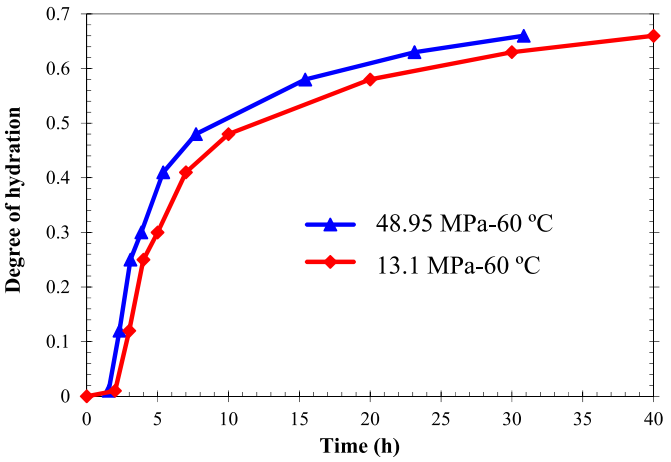

Fig. 4. Degree of hydration vs time relationship at a reference (13.1 MPa, 60 °C) and the scaled (48.95 MPa, 60 °C) case.

In their experiment, the used cement paste was Portland Type G with Silica flour (35% BWOC) and bentonite (0.5% BWOC). A w/c ratio of 0.62 was used for the preparation of the slurry. The hydration took place under atmospheric pressure and at a temperature of 110 °C for 5 days. The hollow cylinder rock was the Berea sandstone with a Young's modulus of 13 GPa. The Young's modulus of the cement was set to be 8 GPa. More details about the experiment can be found in Vrålstad et al. (2019). Fig. 5 shows the scanned image of the test for the casing pressure at 0 and 32 MPa. Initially, no visible defect was observed in the cement

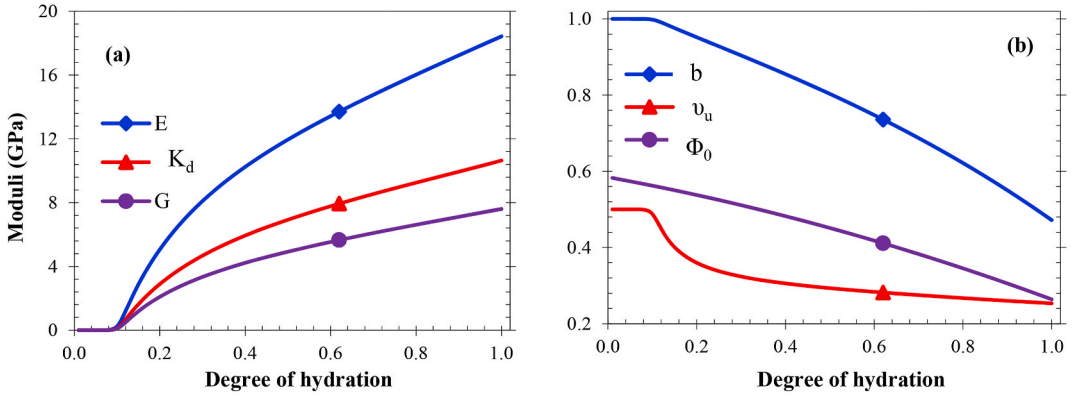

Fig. 3. Some simulated poroelastic parameters of a hydrating class H cement paste with w/c equal to 0.38 using the multiscale micromechanics model and homogenization method.

and rock, but a radial fracture developed as the pressure was increased to 32 MPa.

A 2D plane-strain and quarter model of the sample was simulated using the MDEM code. In contrast to the experiment, the pressure was increased step-by-step without any pressure release in each step. This loading path was followed because the code does not capture the cyclic behavior of materials. The tensile strength of the cement and rock was set in such a way that the fracture pattern would be similar to that of the experiment at the corresponding pressure. A previous similar analysis showed that to reproduce similar results, one must use a random distribution of tensile strength (Gheibi et al., 2019). A normal distribution of tensile strength is given by $T = 9 + 1.5 \times randn$ (in MPa), with *randn* being the standard normal distribution generator. A constant value of 15 MPa was used as the tensile strength of the rock. Fig. 6 shows the displacement field, and a radial fracture formed at a casing pressure of 32 MPa, which is comparable to the experimental result presented in Fig. 5.

Even though the experiment presented by Vrålstad et al. (2019) was performed under zero confinement, our model was tested under several confining pressures, which were applied at the external boundary of the rock. Fig. 7 shows the fracture patterns for confining pressures of 5 and 13.5 MPa, as well as under different casing pressures (Pw). Based on the results obtained and shown in this figure, the casing pressure required to develop radial fractures increases for higher confining pressures. At a higher confinement, the increase in the casing pressure leads to more radial fractures being contained only in the cement. However, under lower confinement, the increase in the casing pressure can lead to fracture propagation into the rock.

4.2. Simulation of a field case example

Cooke et al. (1983) performed a field study and measured the annular pressure and temperatures of hydrating cement pastes at different depths and in different wells. In this paper, we only focus on the pressure data in one of the wells (well A in Cooke et al., 1983). Fig. 8 shows the pressure and temperature measured in the well at different depths, with position 1 being at the downhole (at 2668 m) and position 6 being closest to the surface (at 1108 m). The annular pressure increased during the pumping (placement) of cement slurry and started to decline after complete pumping. However, the temperature started to increase much later, and this increase is related to the high heat released during cement setting.

Several casing sizes were used in our analyses. It was also assumed that the rock formation is a Berea sandstone with a Young modulus (E) of 13 GPa and a Poisson ratio (v) of 0.31 (Makhnenko et al., 2016), and the

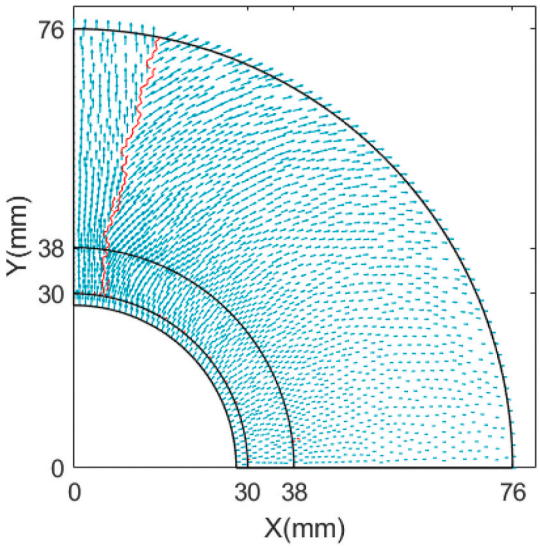

Fig. 6. Displacement field and the fracture formed at the casing pressure of 32 MPa.

casing has E = 200 GPa and v = 0.27. A softer rock formation scenario is also presented.

4.2.1. Well model construction

Fig. 9 shows a quarter model of the well built in MDEM. The left and bottom boundaries of the model are fixed in the x and y directions, respectively. The top and right boundaries are stress boundaries, where the horizontal stresses are applied. The fluid pressures are also assigned to the corresponding cement and rock domains. The well pressure is applied as tractions on the inner wall of the casing. Mud or slurry pressure is also applied as traction before the casing and cement domains are activated. The external boundary is sufficiently large (3 × 3 m), ensuring that the boundary does not affect the analysis significantly.

4.2.2. Stress analysis

The procedure described in Section 3.2 is followed to obtain the stress state in the cement. The depth of interest is the location of the pressure and temperature sensor 1 in Cooke et al. (1983), i.e., 2670 m. The mud and cement slurry densities were 1198–1234 and 1983 kg/m3, respectively. They calculated the cement top to be at a depth of 366 m. Because the formation pore pressure around the well has not been reported, this formation pore pressure (P_f) was assumed to be 26.7 MPa,

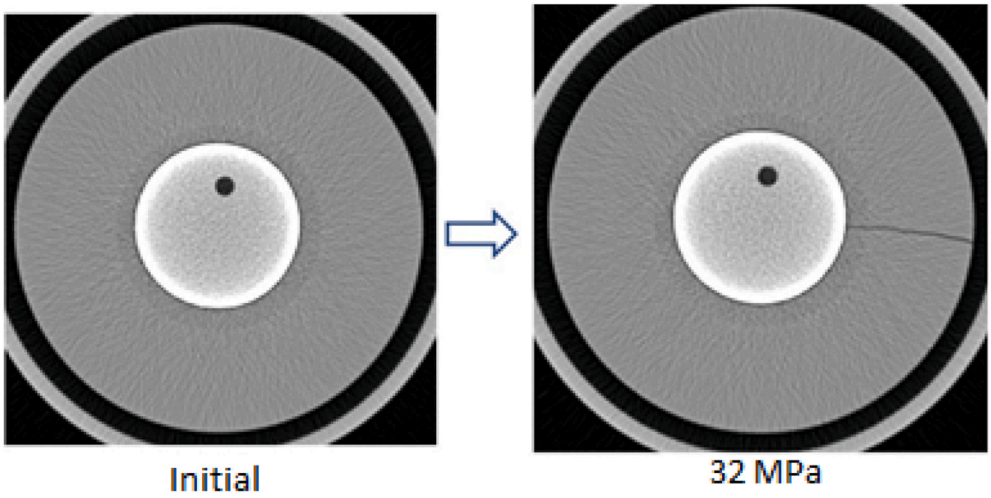

Fig. 5. 2D CT images of sample during pressure cycling, which show the evolution of radial cracks (Vrålstad et al., 2019).

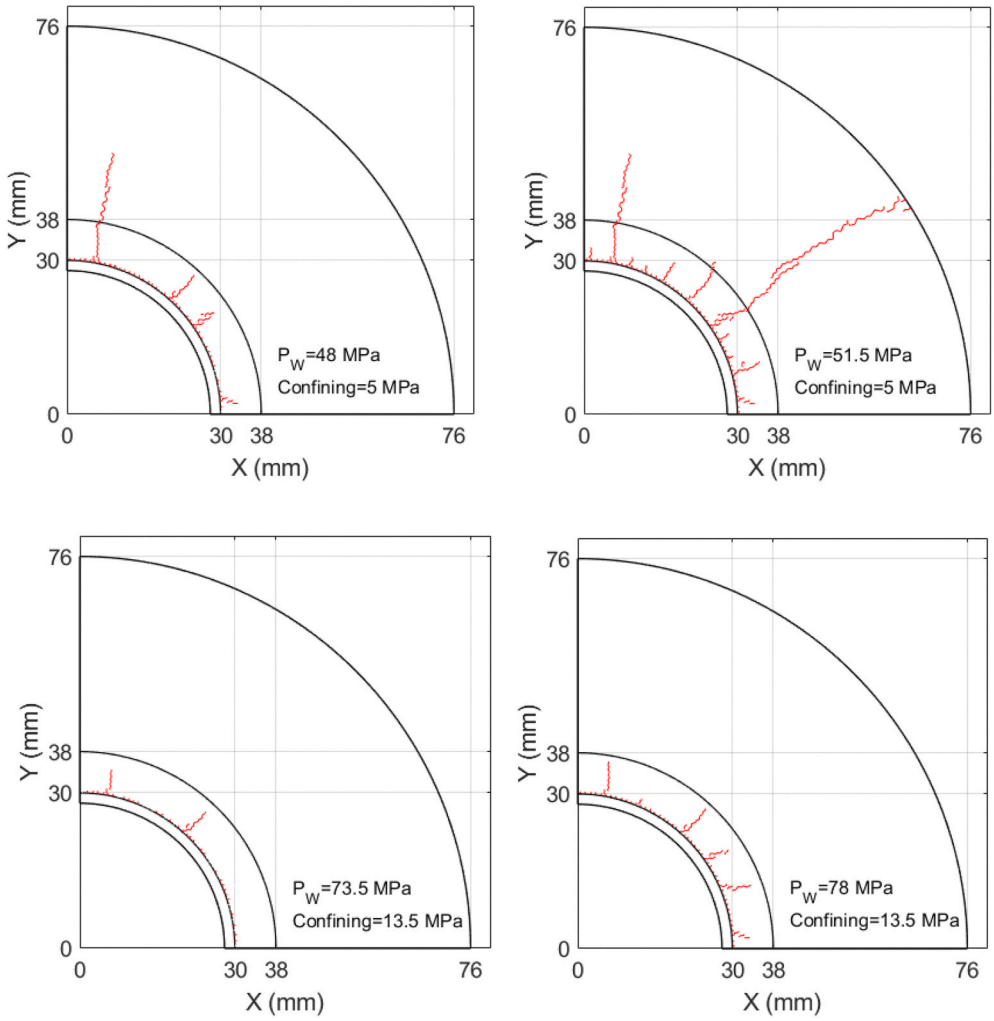

Fig. 7. Radial fracture pattern at different confinement and casing pressure levels.

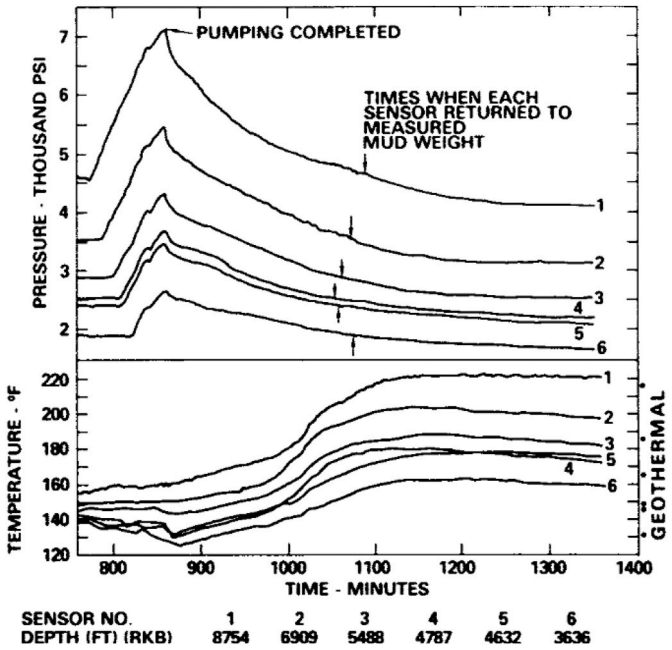

Fig. 8. Annular pressure and temperature vs. time (Cooke et al., 1983).

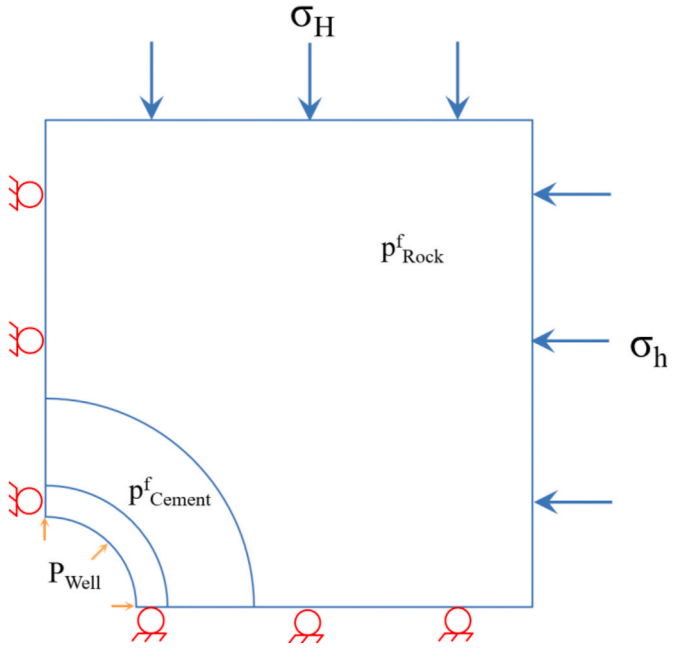

Fig. 9. Schematic view of the model used in the analyses showing the boundary conditions.

corresponding to the hydrostatic value at the considered depth. However, Cooke et al. (1983) reported that the annular pressure approached the formation pore pressure, and the assumed value therefore appears to be suitable. Similarly, there was no information about the in-situ stresses. The horizontal stresses were also assumed to be isotropic. Because they stopped the cement to avoid exceeding the formation fracture pressure, we estimated the horizontal stress using the following relation (Fjaer, 2008):

$$\sigma_h = \frac{P_{frac} + P_f}{2} \tag{12}$$

where σ_h, P_{frac}, and P_f are the total horizontal stress, fracture pressure (here, the cement slurry column pressure), and formation pore pressure, respectively. P_{frac} was estimated to be 53 MPa, which corresponds to the case the entire depth 2670 m is filled with cement (e.g. cement top at a depth zero). Using Eq. (12), the total horizontal stress was estimated to be 40 MPa. The mud pressure was also 32 MPa at the depth of interest. According to Figs. 3 and 8, from $\xi = 0$ to 0.1, the cement paste is in the hydration stage usually known as dormant period, where it starts losing its ability to transmit the pressure, but has not yet form a solid structure with stresses. Therefore, at this stage, only the pressure declines in the model, and no effective stress is developed in the cement. However, the surrounding formation and the casing experience unloading and change in the stress state due to the decline in the cement pore pressure. From $\xi > 0.1$, the cement sets and starts to solidify, and the poroelastic parameters start to change as well as decline in pressure. While the pressure declines in the cement, the effective stress increases and becomes compressive (positive). The decline of the pore pressure of the cement also affects the stress state in the formation. Fig. 10-a-b shows the evolution of the effective radial and tangential stresses in the cement and the formation along the horizontal direction (plane $\theta = 0$). The effective radial stress starts to increase from zero as the hydration continues and reaches ~7 MPa at $\xi = 0.6$. In contrast, the effective radial stress decreases in the formation because of the unloading of the formation as the pressure in the annulus decreases. From $\xi = 0$ to 0.1, there is a dramatic drop in the value of σ_r', but it is less dramatic for $\xi > 0.1$. The reason is that the decline in the pressure is more dramatic, as shown in Fig. 8 (measured pressure). Similarly, the effective tangential stress increases from zero in the cement as the hydration proceeds, and it also increases in the rock formation.

Fig. 11 shows the Mohr circle at the vicinity of the casing-cement interface corresponding to the most unstable location in the cement as it presents a better illustration of the stress state than the stress profile. As shown in the figure, the shear stress develops in the cement and is greater in higher degree of hydration. However, it is important to note that in this example, the shear stress that is developed is not very high, but it is likely that it would be greater if the pressure in the cement decreased further.

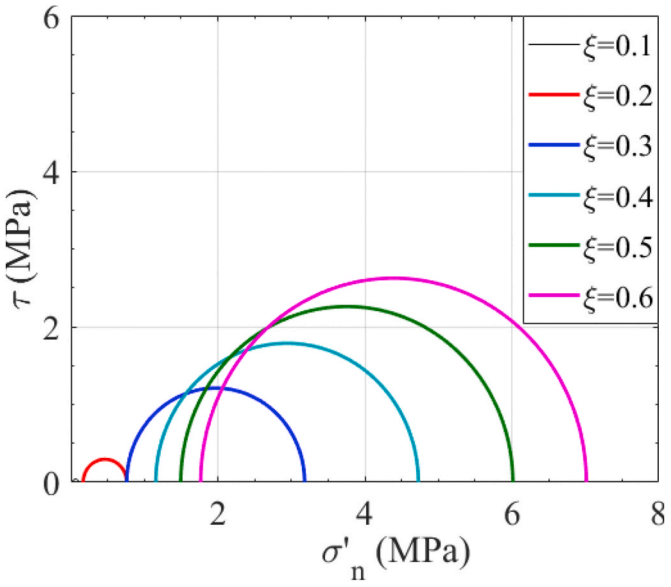

Fig. 11. Mohr circles in the cement sheath corresponding to different values of ξ.

4.2.3. *Well pressure decrease*

The current stresses in the casing, cement, and formation were estimated before performing any operation. The pressure in the casing can decrease owing to changes in the mud during the completion stages. Therefore, it is important to check the casing-cement-rock system integrity because of decreased pressure. To do this, we decreased the well pressure from the mud pressure of 32 MPa–10 MPa ($\Delta P = -22$ MPa), and from 32 MPa to 0 MPa ($\Delta P = -32$MPa) after the cement reached $\xi = 0.5$. Fig. 12 shows the effective radial stress in the cement and formation domains before and after the well pressure reduction.

As expected, the stress can become tensile (negative), and it is more dramatic in the casing-cement interface (−3 MPa) compared to the cement-formation interface (−0.5 MPa). This can lead to the formation of microannuli. Debonding can occur if the tensile radial stress exceeds the tensile strength of the interface. It was observed that the radial stress becomes tensile at the casing-cement interface and in cement close to the interface during the reduction of the well pressure (Fig. 12). It was assumed that the tensile strength of the interface is 0 MPa, and because the radial stress was tensile slightly below 0 MPa, debonding occurred for $\Delta P = -22$ MPa. Fig. 13 shows the de-bonded interface at the casing-cement interface. The measured microannuli openings were calculated

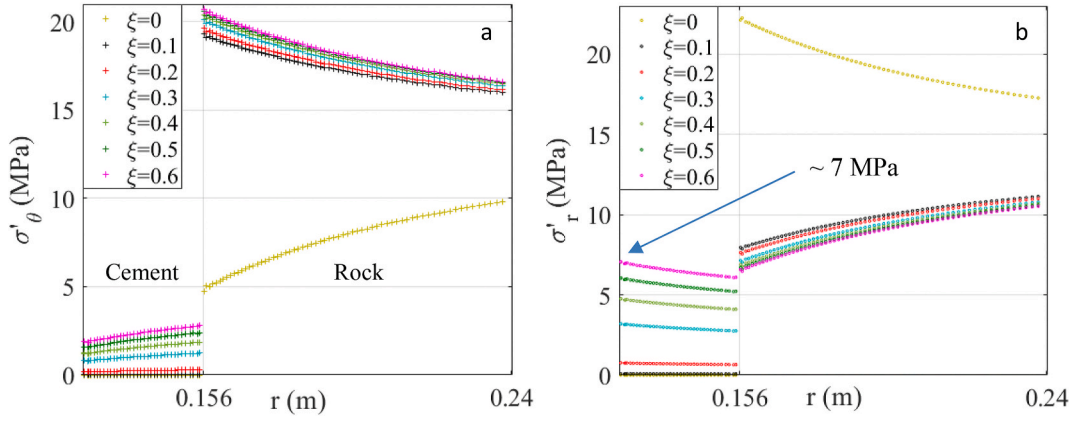

Fig. 10. Plot of effective a) tangential, b) radial stress profiles in the radial direction at different values of ξ.

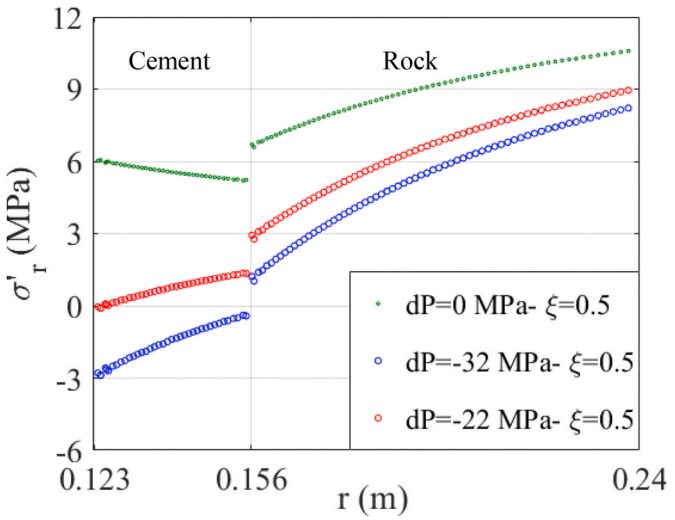

Fig. 12. Effective radial stress along the radial direction for different pressure reductions in the casing.

to be 1.05, 23.76, and 46.5 μm for pressure reductions of $\Delta P = -22$, -27, and -32 MPa, respectively. The opening size is of the same order as that calculated by Boukhelifa et al. (2004) based on lab experiments as well as those calculated by Bois et al. (2011). The interface can open further or close depending on the later loading scenario. The pressure reduction quantity is evidently extreme compared with the real cases. However, because the temperature effect, which is not included here, the pressure was reduced significantly to show that the debonding can occur and that the opening can be estimated using the code.

4.2.4. Well pressure increase

Increase in the well pressure, such as in the pressure test and hydraulic fracturing operation, can lead to cement integrity problems. We solved an example of a pressure increase at $\xi = 0.5$. The casing pressure was increased from 32 MPa (mud pressure) to 44, 54, and 64 MPa (pressures variation $\Delta P = 12$, 22, and 32 MPa, respectively). The cement sheath can fail in tensile or shear conditions depending on the stress and strength level. These two failure mechanisms are investigated separately, as described below.

a Tensile failure

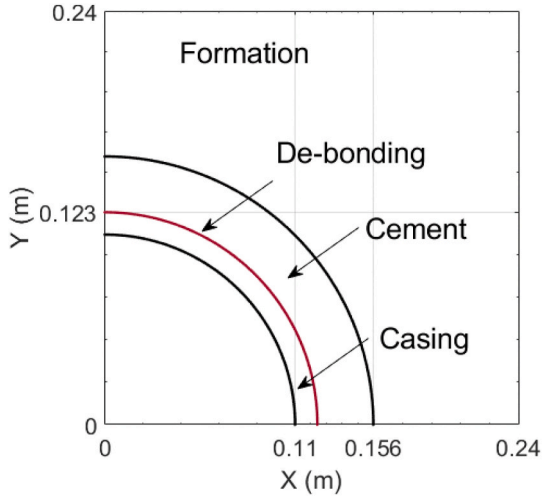

Fig. 13. Debonding of the casing-cement interface owing to a pressure reduction in the casing.

The tensile strength of the cement sheath was randomly generated from $T = 9 + 1.5 \times randn$(in MPa), where *randn* is the standard normal distribution generator. This was obtained from the calibration of the lab-scale model in Section 4.1. The casing was pressurized in increments of 0.1 MPa. Fig. 14 shows the radial fracture evolution at several levels of differential pressure. The number of fractures increases from one to four as the differential pressure ΔP increases from 32.1 to 34 MPa. The figures also show the minimum effective principal stress (σ′3 or the effective tangential stress) in the cement sheath and in the formation. The stress concentration at the tip of the fracture is also visible; however, it is almost zero at its minimum. This means that the fractures may not propagate into the formation. Similar analyses were performed for lower differential pressures, such as 10 MPa. The tensile strength should be 1/3 to create fractures in the cement sheath. We can conclude that the cement sheath to withstand the 20 MPa differential pressure should have a tensile strength of about $T = 6 + 1.5 \times randn$. It is important that the calibrated values are not necessarily the same as values measured in the laboratory.

b Shear failure

The internal friction angle of cement was assumed to be 17° (Bosma et al., 1999), and the cohesion was randomly generated using $C = 13 + 1.5 \times randn$. Fig. 15 shows the shear stress in the xy plane and the evolution of the shear failures in the cement sheath for several differential pressures.

4.3. Effect of casing size

To study the effect of the casing, other casing sizes were tested. Table 1 shows the casing and annulus sizes. The fluid swap (well pressure decrease) was performed for several casing sizes. It was assumed that the debonding occurs if the radial stress becomes just negative. Table 2 shows the required differential pressure to experience debonding at the casing-cement interface. Of the others, casing II is the weakest because it required lowest ΔP to form debonding (i.e. a shift from 32 MPa casing (mud) pressure to 14 MPa caused debonding). However, a decrease of mud pressure from 32 MPa to 5 MPa (i.e. $\Delta P = -27$ MPa) was required for debonding to occur in casing III. The well pressure increase was also tested for these casing sizes. Similarly, casing II is the weakest casing scenario in the pressure increase test as it shows the lowest differential pressure increase to go radial fracture (i.e. $\Delta P = 26.5$ MPa in Table 2).

4.4. Effect of the young modulus of the rock formation

It was assumed that the rock formation is soft (such as Castelgate Sandstone) and has a Young's modulus of 2 GPa (6.5 times softer than the base case). The stress evolution in the cement sheath is different compared to the base case. The reason is that the cement pressure reduction due to the hydration leads to the deformation of the soft rock formation, and results in a smaller decrease in the total stress. Therefore, we observe a shift in the Mohr circle of the cement sheath in the case with a softer formation (Fig. 16). Compared to that of the base case (solid line), the change in shear stress is slightly greater in the soft case.

4.4.1. Well pressure increase

A differential pressure of 30 MPa was applied to the casing in the soft formation model. For comparison, the Mohr circle is as plotted in Fig. 16 in an elastic solution. The cement sheath in the softer formation is more prone to both shear and tensile failure. This is because the soft formation provides less support to the cement sheath, and a greater tensile stress is induced. Fig. 17 shows the fracture evolution in the soft formation model. The cement sheath tensile strength is the same as the base case, but the fracture initiates at a lower differential pressure. Figs. 17 and 14 both show that the number of fractures is greater in the cement sheath,

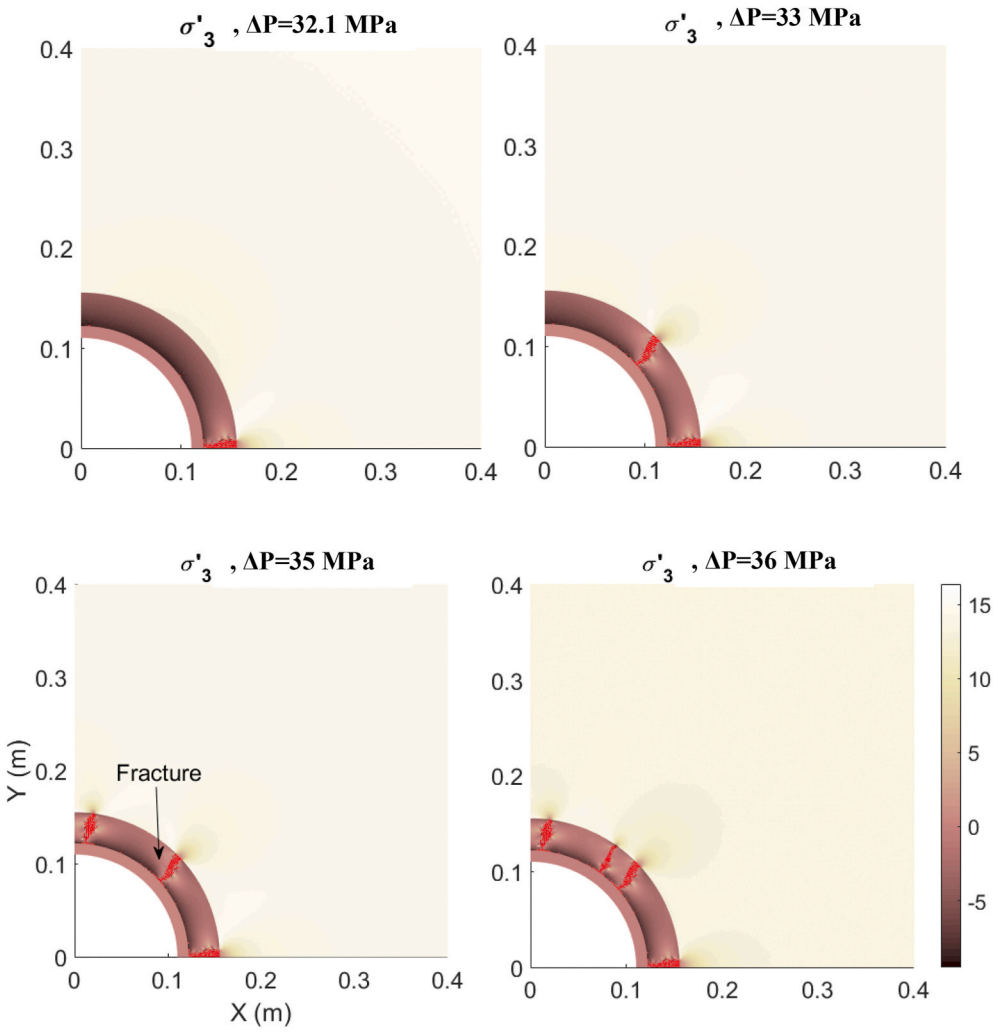

Fig. 14. Distribution of minimum effective principal stress (σ′3) and evolution of the tensile radial fractures as a result of casing pressure increase at $\xi = 0.5$.

and the fractures propagate more slowly in the soft model compared to the stiffer formation case (not visible in the figures).

4.4.2. Well pressure decrease

Fig. 18 shows the radial stress profile in the cement sheath and formation as the well pressure was reduced to zero. In contrast to the base case, the softer formation model does not appear to be suffering from debonding after a fluid swap (i.e. the effective radial stress in this case is positive both in cement and in rock for the two considered differential pressures).

4.5. Effect of loading time

As described in section § 3, the properties of cement paste evolve with time. Therefore, the time at which the cement is loaded is important. In this section, the pressure in the casing is changed at different degrees of hydration, such as 0.2, 0.35, 0.5, and 0.65 which are respectively equivalent to 3, 4.5, 9, and 28 h after cement pumping was stopped based on Fig. 8 and combining with Fig. 4.

4.5.1. Well pressure decrease

The pressure in the casing was reduced to 10 MPa, and the effective radial stresses are shown in Fig. 19. The figure implies that the debonding is more likely at lower values of ξ, and even the cement-casing interface is still under compression at $\xi = 0.65$.

4.5.2. Well pressure increase

The well pressure was increased from 32 to 64 MPa at different values of ξ. The tangential stress induced in the cement sheath was greater (tensile) at higher ξ. At the same time, the cement strength increases with hydration. Therefore, it is difficult to determine whether it becomes more or less stable. Fig. 20 shows the dimensionless compressive strength of cement (Portland) vs ξ at different w/c ratios based on experimental and theoretical studies (Taplin, 1959; Pichler and Hellmich, 2011). This figure was used to approximate the ratio of the tensile and shear strengths over the stresses induced in the cement at different values of ξ and is shown in Fig. 21. The values presented in Fig. 21 are only for a relative comparison, the exact numbers do not convey real meanings because they have been normalized by an assumed final developed stress (15 and 20 MPa in tangential and radial directions) in the cement at different values of ξ. Further, the tensile strength was assumed to be 1/10 of the compressive strength, which may be inaccurate. Fig. 21 implies that the ratio of the strength to the stress is lower in the early stages of cement aging (after the cement is solid). Therefore, both the tensile and compressive failures are more likely in early stages compared to the later stages after the cement has become solid and experiences casing expansion. It is important to note that these speculations are based on approximations, and further detailed numerical and experimental work should be conducted to better understand this behavior.

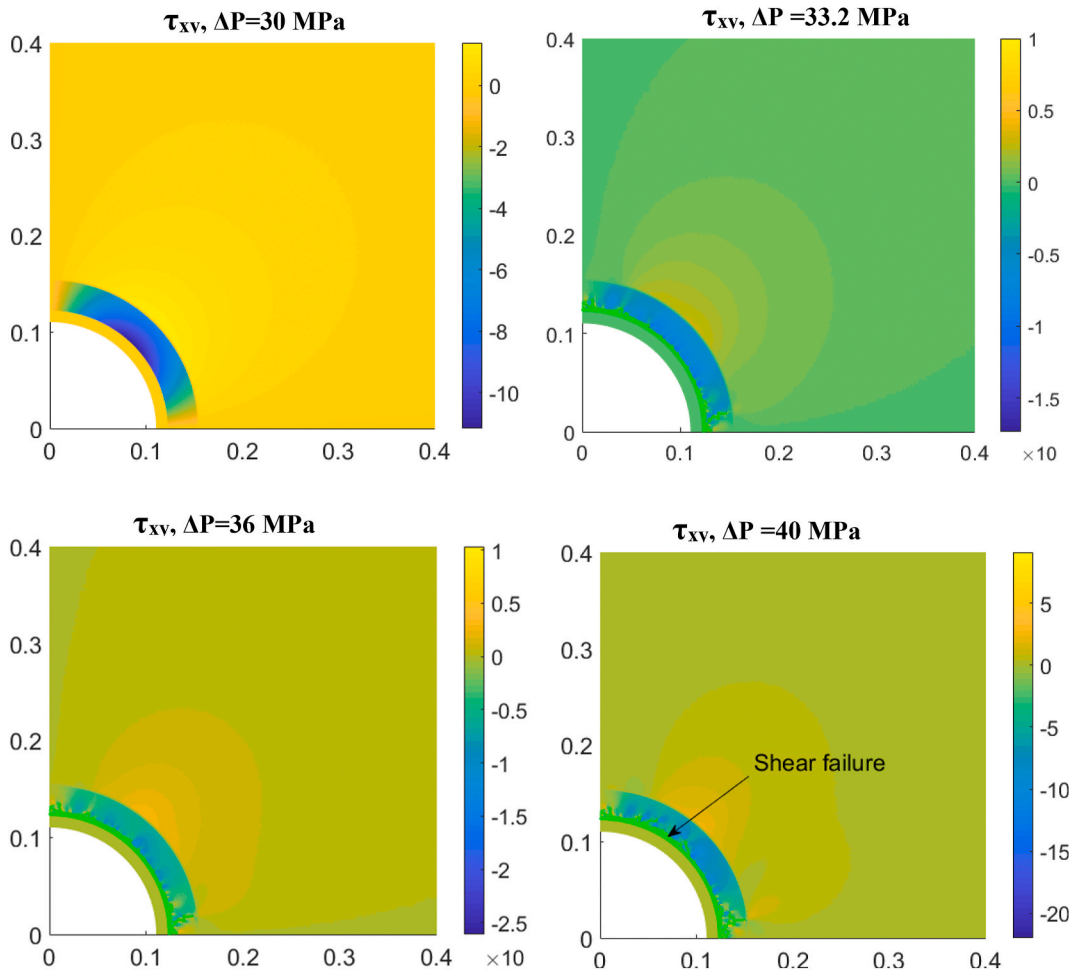

Fig. 15. Distribution of shear stress and evolution of shear failure (in the cement) as a result of casing pressure increase at $\xi = 0.5$.

Table 1
Hole and casing sizes used in the analyses.

Cases	Hole diameter	Casing OD	Casing thickness	Cement thickness
Casing I (C62)	12 ¼" (311.15 mm)	9 5/8" (244.5 mm)	12.0 mm	33.325 mm
Casing II (C65)	12 ¼" (311.15 mm)	9 5/8" (244.5 mm)	8.9 mm	33.325 mm
Casing III (C63)	12 ¼" (311.15 mm)	9 5/8" (244.5 mm)	15.1 mm	33.325 mm
Casing IV (C51)	8 ½" (215.9 mm)	7" (177.8 mm)	12.6 mm	19.05 mm

Table 2
Cement failure pressure corresponding to different operations for used casing sizes.

Operation	Failure mechanism	Casing	I	II	III	IV
Well pressure decrease	Debonding	ΔP (MPa)	−22	−18	−27	−28
Well pressure increase	Radial fracture	ΔP (MPa)	32.1	26.5	47.1	43.1

5. Conclusion

In this investigation, we performed a numerical analysis of cement sheath stability using the modified discrete element method (MDEM), which treats materials as porous media. Field-measured cement pressure data (measured by Cooke et al., 1983) were used in the analyses to estimate the stress state that evolved in the cement during the hydration. The poroelastic parameters of class H cement paste during its hydration were estimated using multiscale micromechanics models coupled with homogenization techniques. The results showed that the pressure

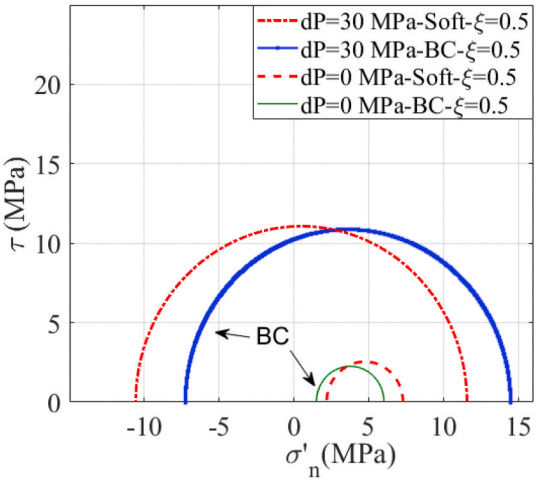

Fig. 16. Comparison of Mohr circles in the cement domain for the base case (BC) and soft formation under pressure increase operation (elastic solution).

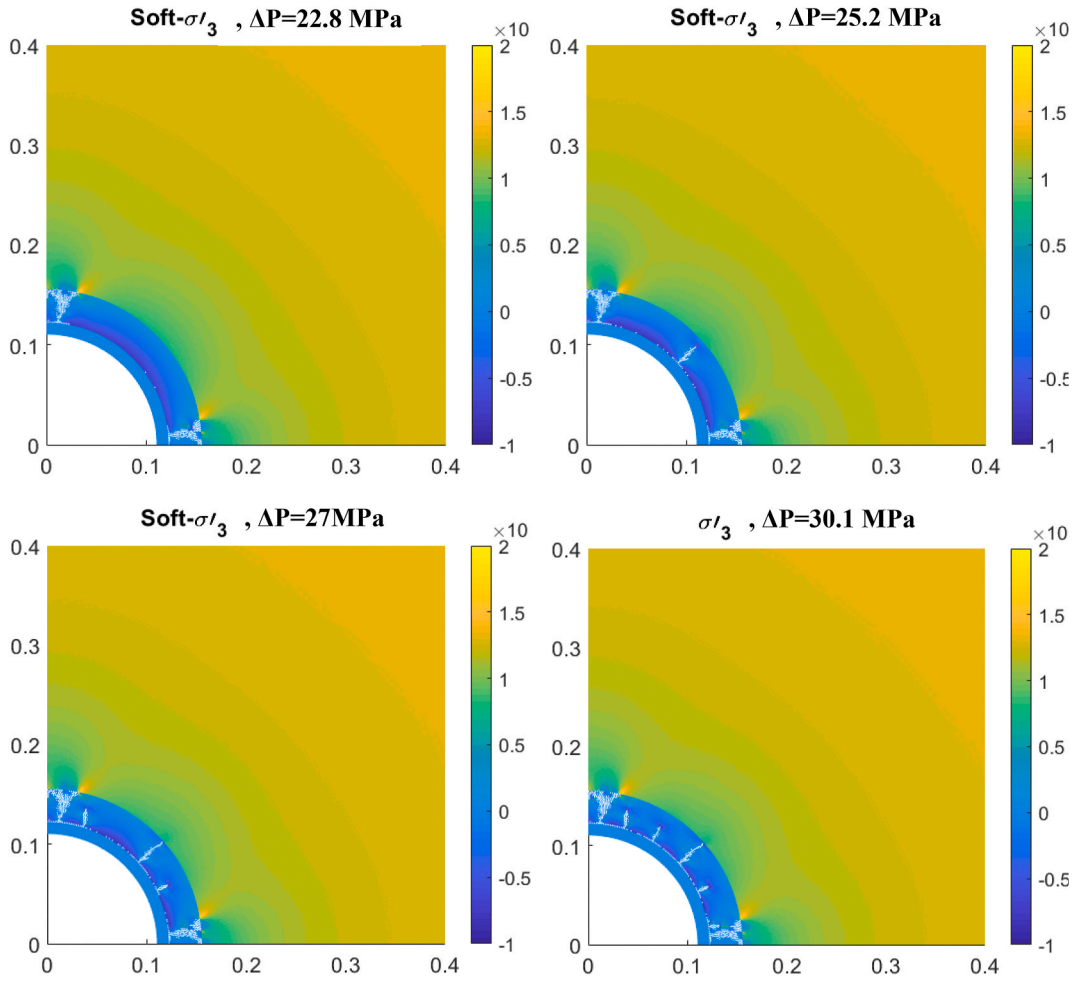

Fig. 17. Distribution of minimum principal stress and evolution of tensile radial fractures (in the cement) as a result of a casing pressure increase at $\xi = 0.5$ for the soft formation case.

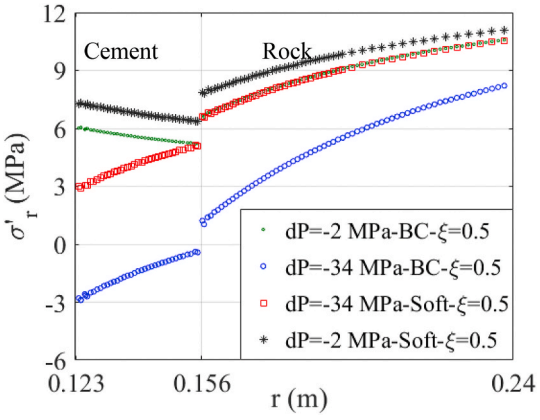

Fig. 18. Comparison of effective radial stress along the radial direction for different pressure reduction in the casing for the base and soft formation cases.

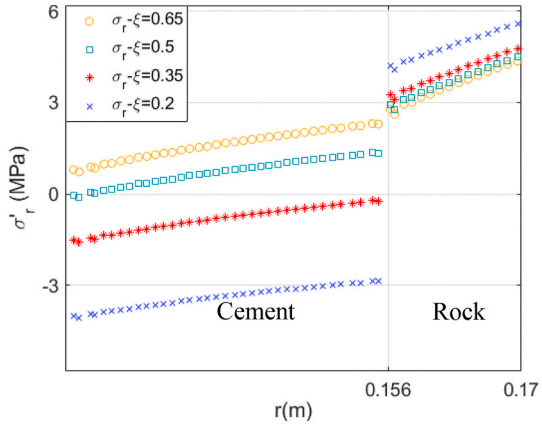

Fig. 19. Effective radial stress along the radial direction for dP = −22 MPa (pressure reduction) in the casing at different degrees of hydration.

decline in the cement slurry leads to compaction of the cement, increases the effective stresses in the cement and change the total stresses in the surrounding. The stress profiles were calculated at different degree of hydration after the percolation threshold.

The well system underwent several pressure-change scenarios that simulated the pressure test, injection, and fluid change. An increase in the well pressure was shown to potentially cause radial fractures and shear failure in the cement. The failures were progressive, which implies that they evolved as the loading condition changed. Based on the analyses, the failures occurred only in the cement sheath and further loading did not propagate the fractures into the rock formation. Debonding occurred in the casing-cement interface as the pressure decreased in the well. The interface opening varied depending on the degree of pressure decrease and ranged from 1 to 50 μm in our simulations. Debonding, radial and shear failures are more likely in the cement at lower degree of

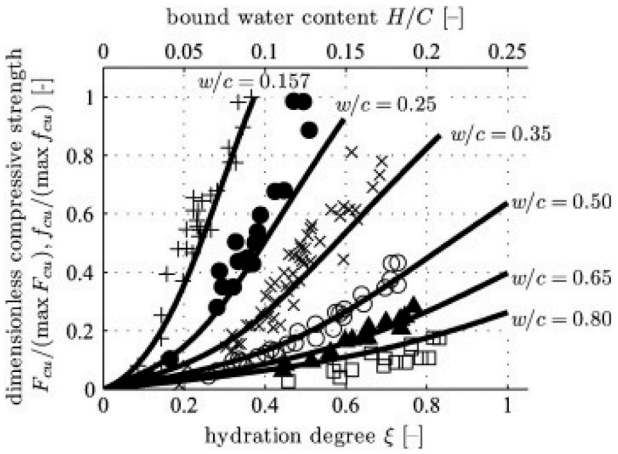

Fig. 20. Strength evolution of hydrating cement pastes: experimental results of Taplin (1959) and predictions of the proposed model by (Pichler and Hellmich, 2011).

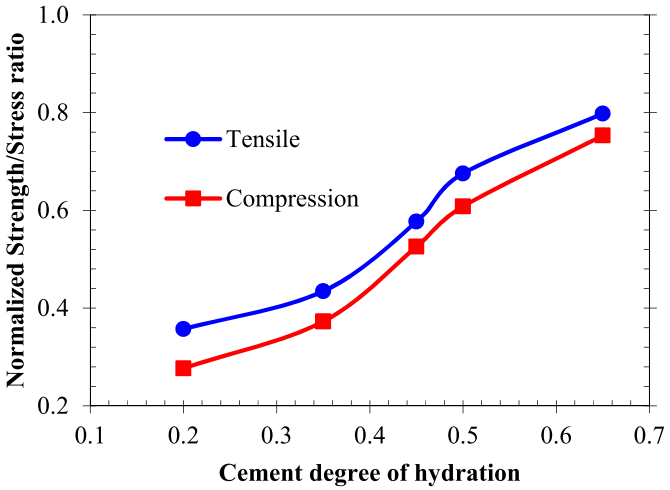

Fig. 21. Normalized strength/stress ratio of a hydrating cement paste.

hydration when it is solid. Moreover, there was no debonding in the model with the softer rock formation. However, there was radial fracture for a lower pressure increase in the cement sheath for the stiffer case. Smaller diameters and thicker casing are conditions that result in greater robustness to cement sheath damage owing to radial and debonding failures.

CRediT authorship contribution statement

Sohrab Gheibi: Conceptualization, Methodology, Software, Validation, Formal analysis, Investigation, Writing - original draft, Visualization, Project administration. **Nicolaine Agofack:** Methodology, Investigation, Writing - original draft, Visualization, Formal analysis. **Sigbjørn Sangesland:** Writing - review & editing, Supervision, Funding acquisition.

Declaration of competing interest

The authors declare that they have no known competing financial interests or personal relationships that could have appeared to influence the work reported in this paper.

Acknowledgement

The authors acknowledge the Research Council of Norway, AkerBP, ConocoPhilips, Equinor and Wintershall for financing the work through the DrillWell research centre- Drilling and Well Centre for Improved Recovery, a research cooperation between NORCE, NTNU, SINTEF and UiS. The authors also acknowledge the SECURe project.

Appendix A. Supplementary data

Supplementary data to this article can be found online at https://doi.org/10.1016/j.petrol.2020.107720.

AppendixModified Discrete Element Method

The modified discrete element method (MDEM) was proposed by Alassi (2008) to model the failure of geomaterials in the context of reservoir geomechanics. It has also been used in the modeling of reservoir pressurization, hydraulic fracturing, as well as fault reactivation. MDEM is a hybrid code that captures both continuum and discontinuum features of materials' behavior. A triangle element (continuum) is made of the centers of three particles that are connected by springs. A force is transmitted when a relative displacement occurs between the particles. In the elastic regime, the solution is continuum, but as soon as an element fails, the fractures appear as a breakage of the springs, which can open, close, or slide depending on the loading condition. Figure A. 1 shows a triangular element formed by connecting the centers of three discs that are in contact with each other.

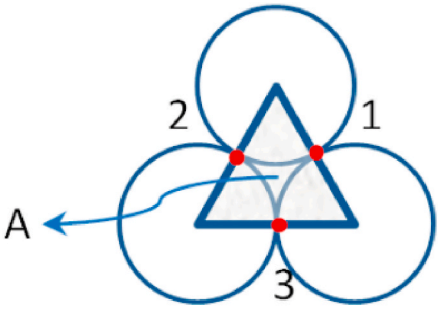

Fig. A.1. Representation of an element in MDEM. The red dots show the contacts/fractures and their allocated ID (Alassi, 2008).

A contact force is calculated using Eq. (A.1):

$$\mathbf{F} = \mathbf{Kd} \tag{A.1}$$

where F represents the internal forces, K is the micromechanical constitutive matrix, and d is the relative displacement of the contact. The relationship between the stress and the internal forces, as well as the relation between the strain and the nodal (triangle vertex) displacements, is given by:

$$\boldsymbol{\sigma} = \frac{1}{A}\mathbf{M}^{\mathrm{T}}\mathbf{F} \tag{A.2}$$

$$\mathbf{U} = \mathbf{M}\boldsymbol{\varepsilon} \tag{A.3}$$

where A, M, and ε are the area of the triangle, the unit normal matrix, and the strain, respectively. The stress is related to the strain by using the material conventional constitutive elastic matrix C given in Eq. (A.4):

$$\boldsymbol{\sigma} = \mathbf{C}\boldsymbol{\varepsilon} \tag{A.4}$$

Combining Eqs. (A.1)–(A.4), the micromechanical constitutive matrix K can be evaluated from the following relation:

$$\mathbf{C} = \frac{1}{A}\mathbf{M}^{\mathrm{T}}\mathbf{K}\mathbf{M} \tag{A.5}$$

The code adopts the second law of Newton and uses an explicit scheme for positions of the particle, so the internal forces are calculated incrementally (Cundall and Strack, 1979). When the stress value reaches the strength threshold, the elements fail by breaking two of the springs, which are under the critical load. The normal and shear forces of the contacts are also updated after failure, depending on the loading condition. The code adopts a Mohr-Coulomb failure criterion with a cut-off. The solution is equivalent to a linear finite element in an elastic regime, and to a regular discrete element after the element has failed. The code assumes that the material is isotropic-linear-elastic-brittle and no softening occurs during the spring separation.

References

Agofack, Nicolaine, Ghabezloo, Siavash, Jean, Sulem, 2020. Chemo-poro-elastoplastic modelling of an oilwell cement paste: macroscopic shrinkage and stress-strain behaviour. Cement Concr. Res. 132, 106046. https://doi.org/10.1016/J.CEMCONRES.2020.106046. June.

Agofack, Nicolaine, Ghabezloo, Siavash, Jean, Sulem, Garnier, André, Urbanczyk, Christophe, 2019. Experimental investigation of the early-age mechanical behaviour of oil-well cement paste. Cement Concr. Res. 117, 91–102. https://doi.org/10.1016/j.cemconres.2019.01.001. March.

Alassi, 2008. Modeling Reservoir Geomechanicsusing Discrete Element Method: Application to Reservoirmonitoring. NTNU. https://brage.bibsys.no/xmlui/handle/11250/239293.

Arjomand, Elaheh, Bennett, Terry, Nguyen, Giang D., 2018. Evaluation of cement sheath integrity subject to enhanced pressure. J. Petrol. Sci. Eng. 170, 1–13. https://doi.org/10.1016/J.PETROL.2018.06.013. November.

Bensted, John, 1998. Special cements. In Lea's Chemistry of Cement and Concrete. Butterworth-Heinemann, pp. 783–840. https://doi.org/10.1016/B978-075066256-7/50026-6.

Bernard, O, Ulm, F, Lemarchand, E, 2003. A multiscale micromechanics-hydration model for the early-age elastic properties of cement-based materials. Cem. Conc. Res.

Bois, A, Garnier, A, Rodot, F, Sain-Marc, J, Almard, N, 2011. How to prevent loss of zonal isolation through a comprehensive analysis of microannulus formation. SPE Drill. Compl.

Bois, Axel-Pierre, Vu, Manh-Huyen, Kim, Noël, Anthony, Badalamenti, Delabroy, Laurent, Thérond, Emmanuel, Hansen, Knut, 2019. Evaluating Cement-Plug Mechanical and Hydraulic Integrity. SPE Drilling & Completion. https://doi.org/10.2118/191335-PA. February.

Bosma, Martin, Ravi, Kris, Willem van Driel, Jan Schreppers, Gerd, 1999. Design approach to sealant selection for the life of the well. In SPE Annual Technical Conference and Exhibition. Society of Petroleum Engineers. https://doi.org/10.2118/56536-MS.

Boukhelifa, L., Moroni, N., James, S.G., Le Roy-Delage, S., Thiercelin, M.J., Lemaire, G., 2004. Evaluation of cement systems for oil and gas well zonal isolation in a full-scale Annular geometry. In: IADC/SPE Drilling Conference. Society of Petroleum Engineers. https://doi.org/10.2118/87195-MS.

Bu, Yuhuan, Tian, Leiju, Guo, Bingliang, Wang, Chunyu, Sun, Baojiang, 2020. Experiment and simulation on the integrity of cement ring interface in deep water shallow formation. J. Petrol. Sci. Eng. 190, 107127. https://doi.org/10.1016/J.PETROL.2020.107127. July.

Cooke, C.E., Kluck, M.P., Medrano, R., 1983. Field measurements of annular pressure and temperature during primary cementing. J. Petrol. Technol. 35 (8), 1429–1438. https://doi.org/10.2118/11206-PA.

Cundall, P.A., Strack, O.D.L., 1979. A discrete numerical model for granular assemblies. Geotechnique 29 (1), 47–65. https://doi.org/10.1680/geot.1979.29.1.47.

Dormieux, L, Kondo, D, Ulm, F, 2006. Microporomechanics. John Wiley & Sons.

Fjaer, Erling, 2008. Petroleum Related Rock Mechanics. In: Amsterdam (Ed.). Elsevier. https://www.worldcat.org/title/petroleum-related-rock-mechanics/oclc/928976168.

Fourmaintraux, Dominique M., Axel-Pierre, Bois, Christophe, franco, Bernard, Fraboulet, Pierre, brossolllet, 2005. Efficient wellbore cement sheath design using the SRC (system response curve) method. In: SPE Europec/EAGE Annual Conference. Society of Petroleum Engineers. https://doi.org/10.2118/94176-MS.

Ghabezloo, Siavash, 2010. Multiscale modeling of the poroelastic properties of various oil-well cement pastes. J. Multiscale Model. (JMM) 2, 199–215. https://doi.org/10.1142/S1756973710000412, 03n04.

Gheibi, Sohrab, Sangesland, Sigbjørn, Vrålstad, Torbjørn, 2019. Numerical modeling of radial fracturing of cement sheath caused by pressure tests. In: In Proceedings of the International Conference on Offshore Mechanics and Arctic Engineering - OMAE, 8, pp. 1–7. https://doi.org/10.1115/OMAE2019-96319. Glas.

Gholami, Raoof, Brent, Aadnoy, Fakhari, Nikoo, 2016. A thermo-poroelastic analytical approach to evaluate cement sheath integrity in deep vertical wells. J. Petrol. Sci. Eng. 147, 536–546. https://doi.org/10.1016/J.PETROL.2016.09.024. November.

Goodwin, K.J., Crook, R.J., 1992. Cement sheath stress failure. SPE Drill. Eng. 7 (4), 291–296. https://doi.org/10.2118/20453-PA.

Gray, Kenneth E., Podnos, Evgeny, Becker, Eric, 2009. Finite-element studies of near-wellbore region during cementing operations: Part I. SPE Drill. Complet. 24 (1), 127–136. https://doi.org/10.2118/106998-PA.

Jackson, P.B., Murphey, C.E., 1993. Effect of casing pressure on gas flow through a sheath of set cement. In: SPE/IADC Drilling Conference. Society of Petroleum Engineers. https://doi.org/10.2118/25698-MS.

Li, Zaoyuan, Zhang, Kai, Guo, Xiaoyang, Liu, Jian, Cheng, Xiaowei, Du, Jianbo, 2016. Study of the failure mechanisms of a cement sheath based on an equivalent physical experiment. J. Nat. Gas Sci. Eng. 31, 331–339. https://doi.org/10.1016/J.JNGSE.2016.03.037. April.

Makhnenko, Roman, Y., Labuz, Joseph F., 2016. Elastic and inelastic deformation of fluid-saturated rock. Philos. Tran. Ser. Math. Phys. Eng. Sci. 374 https://doi.org/10.1098/rsta.2015.0422, 2078.

Pang, Xueyu, 2011. Effects of Curing Temperature and Pressure on the Chemical, Physical, and Mechanical Properties of Portland Cement. https://doi.org/10.7916/D8RF620F.

Pichler, Bernhard, Hellmich, Christian, 2011. Upscaling quasi-brittle strength of cement paste and mortar: a multi-scale engineering mechanics model. Cement Concr. Res. 41 (5), 467–476. https://doi.org/10.1016/J.CEMCONRES.2011.01.010.

Ravi, K., Bosma, M., Gastebled, O., 2002. Improve the economics of oil and gas wells by reducing the risk of cement failure. In: IADC/SPE Drilling Conference. Society of Petroleum Engineers. https://doi.org/10.2118/74497-MS.

Samudio, Marcos, 2017. Modelling of an Oil Well Cement Paste from Early Age to Hardened State : Hydration Kinetics and Poromechanical Behaviour Thèse. UNIVERSITE PARIS-EST. https://pastel.archives-ouvertes.fr/tel-01781441.

Skorpa, Ragnhild, Øia, Thomas, Ali, Taghipour, Vrålstad, Torbjørn, 2018. Laboratory set-up for determination of cement sheath integrity during pressure cycling. In: Polar and Arctic Sciences and Technology, vol. 8. Petroleum Technology, V008T11A039. ASME. https://doi.org/10.1115/OMAE2018-78696.

Skorpa, Ragnhild, Werner, Benjamin, Vrålstad, Torbjørn, 2019. Effect of mud on cement sheath integrity. In: SPE Norway One Day Seminar. Society of Petroleum Engineers. https://doi.org/10.2118/195625-MS.

Taplin, J.H., 1959. A method for following the hydration reaction in Portland cement paste.

Therond, Emmanuel, Axel-Pierre Bois, Whaley, Kevin, Murillo, Rodriguo, 2017. Large-scale testing and modeling for cement zonal isolation in water-injection wells. SPE Drill. Complet. 32 (4), 290–300. https://doi.org/10.2118/181428-PA.

Thiercelin, M., Baumgarte, C., Guillot, D., 1998a. A soil mechanics approach to predict cement sheath behavior. In: SPE/ISRM Rock Mechanics in Petroleum Engineering. Society of Petroleum Engineers. https://doi.org/10.2118/47375-MS.

Thiercelin, M.J., Bernard, Dargaud, Baret, J.F., Rodriquez, W.J., 1998b. Cement design based on cement mechanical response. SPE Drill. Complet. 13 (4), 266–273. https://doi.org/10.2118/52890-pa.

Vrålstad, Torbjørn, Skorpa, Ragnhild, Werner, Benjamin, 2019. Experimental studies on cement sheath integrity during pressure cycling. In: SPE/IADC International Drilling Conference and Exhibition. Society of Petroleum Engineers. https://doi.org/10.2118/194171-MS.

Vu, Manh-Huyen, Axel-Pierre Bois, Anthony, Badalamenti, 2018. Gas migration modeling to prevent sustained casing pressure and casing vent flow. In: SPE/IADC Middle East Drilling Technology Conference and Exhibition. Society of Petroleum Engineers. https://doi.org/10.2118/189384-MS.

Wang, W., Dahi Taleghani, A., 2017. Impact of hydraulic fracturing on cement sheath integrity; A modelling approach. J. Nat. Gas Sci. Eng. 44, 265–277. https://doi.org/10.1016/J.JNGSE.2017.03.036. August.

Wise, Jarrett, Cedola, Alexandra, Nygaard, Runar, Hareland, Geir, Arild, Øystein, Lohne, Hans Petter, Eric Patrick Ford, 2020. Wellbore characteristics that control debonding initiation and microannuli width in finite element simulations. J. Petrol. Sci. Eng. 191, 107157. https://doi.org/10.1016/J.PETROL.2020.107157. August.